







Cite this: *Mater. Adv.*, 2023,  
4, 1021

# Synthesis, structure and electrochemical properties of a new cation ordered layered Li–Ni–Mg–Mo oxide†

Bo Dong, \*<sup>ab</sup> Javier Castells-Gil, <sup>ab</sup> Pengcheng Zhu, <sup>bc</sup> Laura L. Driscoll, <sup>ab</sup> Emma Kendrick, <sup>bc</sup> Phoebe K. Allan<sup>ab</sup> and Peter R. Slater \*<sup>ab</sup>

Lithium-rich oxides are attracting intense interest as the next generation cathode materials for lithium-ion batteries due to their high theoretical capacity. Nevertheless, these materials suffer from a number of shortcomings, such as oxygen loss at high voltage, large hysteresis and poor rate capability. In this work, we show that through a dual cation substitution strategy replacing Ti with Mo and Mg, the disordered rocksalt (DRS)  $\text{Li}_{1.2}\text{Ni}_{0.4}\text{Ti}_{0.4}\text{O}_2$  is transformed into a new cation ordered layered phase  $\text{Li}_{1.2}\text{Ni}_{0.4}\text{Mo}_{0.2}\text{Mg}_{0.2}\text{O}_2$ , with the high valence dopant  $\text{Mo}^{6+}$  on the (0,0,0) site.  $\text{Li}_{1.2}\text{Ni}_{0.4}\text{Mo}_{0.2}\text{Mg}_{0.2}\text{O}_2$  showed improved performance compared to that of the similarly prepared DRS  $\text{Li}_{1.2}\text{Ni}_{0.4}\text{Ti}_{0.4}\text{O}_2$  material ( $\sim 190 \text{ mA h g}^{-1}$  vs.  $\sim 105 \text{ mA h g}^{-1}$  after 10 cycles, respectively). The characteristics of the electrochemical process were studied using *ex situ* XRD and XAS, which indicated the involvement of both Ni and Mo redox during the cycling as well as the electrochemical instability of the layered phase which changes to a disordered rocksalt phase on cycling.

Received 28th September 2022,  
Accepted 7th January 2023

DOI: 10.1039/d2ma00981a

rsc.li/materials-advances

## Introduction

Lithium-ion batteries (LIBs) are widely used as energy storage resources for portable electronics and electric vehicles due to their high energy densities.<sup>1</sup> Nevertheless, in order to satisfy the consumer demand for the long driving range, systems with increased energy densities are being sought. Considering the much higher theoretical and practical capacities of anode materials, the optimisation of cathode materials is crucial in obtaining improved lithium-ion batteries with overall higher energy densities.<sup>2</sup>

Spinel  $\text{LiMn}_2\text{O}_4$ , olivine  $\text{LiFePO}_4$  and layered  $\text{LiNi}_x\text{Co}_y\text{Mn}_{1-x-y}\text{O}_2$  positive electrode materials have been commercially utilised in rechargeable lithium-ion batteries.<sup>3–6</sup> Lithium excess electrode materials, such as  $\text{Li}_2\text{MnO}_3$ , with higher theoretical capacity have attracted much attention in the last decade.<sup>3,4</sup> Theoretically,  $\text{Li}_2\text{MnO}_3$  should be of limited use as a cathode due to the redox inactive  $\text{Mn}^{4+}$  in the structure. However, practically it has been shown to deliver high reversible capacity during cycling owing to the active redox of oxide ions (anion redox) instead of

traditional transition metal ions. These results have inspired others to investigate Li excess cathode materials to obtain high capacities and understand this anion redox process. Combined spectroscopic studies first observed the formation of localized electron holes on the oxygen ions coordinated by  $\text{Mn}^{4+}$  and  $\text{Li}^+$  during the charge of  $\text{Li}_{1.2}\text{Ni}_{0.13}\text{Co}_{0.13}\text{Mn}_{0.54}\text{O}_2$ .<sup>7</sup> Recently, resonant inelastic X-ray scattering and  $^{17}\text{O}$  magic angle spinning NMR spectroscopy has demonstrated the formation of molecular  $\text{O}_2$ , rather than  $\text{O}_2^{2-}$ , which is trapped in the bulk, albeit a small quantity of  $\text{O}_2$  loss is observed from the surface, accounting for the capacity decay during the anion redox process.<sup>8</sup>

The high capacities achieved ( $> 250 \text{ mA h g}^{-1}$  associated with both cationic and anionic redox chemistry<sup>9–12</sup>) with these materials have therefore meant that lithium-rich oxides are attracting considerable interest as the next generation cathode materials for lithium-ion batteries. Still these materials can suffer from several drawbacks, such as oxygen loss at high voltage, large hysteresis and poor rate capability.<sup>10,13–18</sup> To mitigate these drawbacks, a great deal of research has focused on the development of lithium-rich layered as well as disordered rocksalt cathodes, given the flexibility of these structures to incorporate different cation species.<sup>19,20</sup>

Of interest to the study we report here, the DRS  $\text{Li}_{1.2}\text{Mn}_{0.4}\text{Ti}_{0.4}\text{O}_2$  has been reported to show  $300 \text{ mA h g}^{-1}$  capacity at  $50^\circ\text{C}$  in the first cycle which rapidly decays to  $200 \text{ mA h g}^{-1}$  after six cycles. Its electrochemical performance can be further improved through mechanical ball milling with conductive

<sup>a</sup> School of Chemistry, University of Birmingham, Birmingham B15 2TT, UK.  
E-mail: b.dong@bham.ac.uk, p.r.slater@bham.ac.uk

<sup>b</sup> The Faraday Institution, Harwell Science and Innovation Campus,  
Didcot OX11 0RA, UK

<sup>c</sup> School of Metallurgy and Materials, University of Birmingham,  
Birmingham B15 2TT, UK

† Electronic supplementary information (ESI) available. See DOI: <https://doi.org/10.1039/d2ma00981a>



carbons.<sup>21</sup> Doping on the Mn site with Cr has led to high rate capability associated with non-topotactic reactions (octahedral-to-tetrahedral migration of Cr ions) in both  $\text{Li}_{1.2}\text{Mn}_{0.2}\text{Ti}_{0.4}\text{Cr}_{0.2}\text{O}_2$  and  $\text{Li}_{1.2}\text{Ni}_{0.1}\text{Ti}_{0.5}\text{Cr}_{0.2}\text{O}_2$ .<sup>22</sup> Furthermore, short-range ordering studies have revealed the improved performance of  $\text{Li}_{1.2}\text{Mn}_{0.4}\text{Ti}_{0.4}\text{O}_2$  compared to that of  $\text{Li}_{1.2}\text{Mn}_{0.4}\text{Zr}_{0.4}\text{O}_2$ , which has been attributed to the high number of connected lithium sites and improved lithium diffusion within  $\text{Li}_{1.2}\text{Mn}_{0.4}\text{Ti}_{0.4}\text{O}_2$ .<sup>23</sup> In comparison, the Ni analogue materials,  $\text{Li}_{1.2}\text{Ni}_{0.4}\text{Ti}_{0.4}\text{O}_2$  have been less studied.<sup>24–27</sup> Apart from DRS materials, lithium-rich layered materials have also attracted attention, and a series of layered materials, with a formula of  $\text{Li}_4\text{MM}'\text{O}_6$  ( $\text{M} = \text{Ni}, \text{Fe}$ ;  $\text{M}' = \text{Mo}, \text{Te}, \text{W}$ ) were reported and electrochemically characterised.<sup>9,28–30</sup>

In this work, we have studied the dual cation substitution ( $\text{Mg}^{2+} + \text{Mo}^{6+} \cong 2\text{Ti}^{4+}$ ) in the disordered rocksalt (DRS)  $\text{Li}_{1.2}\text{Ti}_{0.4}\text{Ni}_{0.4}\text{O}_2$  in order to try to improve the overall electrochemical performance of this DRS phase. Interestingly, rather than retaining the DRS structure, we show a change to a cation ordered layered material through this substitution strategy, and here we report the structure of this new system and the electrochemical performance.

## Experimental

### Synthesis

$\text{Li}_2\text{CO}_3$ ,  $\text{Ni}(\text{NO}_3)_2 \cdot 6\text{H}_2\text{O}$ ,  $\text{MoO}_3$ ,  $\text{C}_4\text{H}_2\text{Mg}_5\text{O}_{14} \cdot 5\text{H}_2\text{O}$  were chosen as starting materials.  $\text{Li}_{1.2}\text{Ni}_{0.4}\text{Ti}_{0.4}\text{O}_2$ ,  $\text{Li}_{1.2}\text{Ni}_{0.4}\text{Mo}_{0.2}\text{Mg}_{0.2}\text{O}_2$ , and  $\text{Li}_{1.1}\text{Ni}_{0.6}\text{Mo}_{0.15}\text{Mg}_{0.15}\text{O}_2$  were made through grinding together mixtures of starting materials in a mortar and pestle and heating at  $650\text{ }^\circ\text{C}/12\text{ h}$  with a rate of  $2.5\text{ }^\circ\text{C min}^{-1}$  to fully decompose carbonate, nitrate and hydrate from the starting materials. The mixture was then ball milled (with 10 – 15% excess lithium to compensate the lithium loss at high temperature) for 30 minutes using a Pulverisette 7 planetary ball mill (12 mL  $\text{ZrO}_2$  pots with 10 mm diameter  $\text{ZrO}_2$  balls) to gain fine powders. The powders were pressed into 16 mm diameter pellets at 0.2 tons and reheated at  $900\text{ }^\circ\text{C}/12\text{ h}$  with a rate of  $5\text{ }^\circ\text{C min}^{-1}$  for synthesis. The powders of  $\text{Li}_{1.2}\text{Ni}_{0.4}\text{Mo}_{0.2}\text{Mg}_{0.2}\text{O}_2$ , and  $\text{Li}_{1.1}\text{Ni}_{0.6}\text{Mo}_{0.15}\text{Mg}_{0.15}\text{O}_2$  were further reground and reheated at  $925 - 950\text{ }^\circ\text{C}/12\text{ h}$  with a heating rate of  $5\text{ }^\circ\text{C min}^{-1}$  to gain the final product.

### X-Ray diffraction

X-Ray diffraction (XRD) data were collected using a Bruker D8 X-ray diffractometer with a linear position sensitive detector (PSD) ( $\text{CuK}_\alpha$  radiation). Room temperature XRD patterns were recorded over the  $2\theta$  range  $15^\circ$  to  $80^\circ$  with a  $0.02^\circ$  step size. For Rietveld refinement, data were collected over the  $2\theta$  range  $15^\circ$  to  $120^\circ$  with a  $0.02^\circ$  step size and structure refinement performed using the GSASII suite of Rietveld refinement software.<sup>31</sup>

### Electrochemical characterisation

The active materials and C65 (at the ratio of 9:1) were ball milled at 400 rpm for 2 hours using a Pulverisette 7 planetary

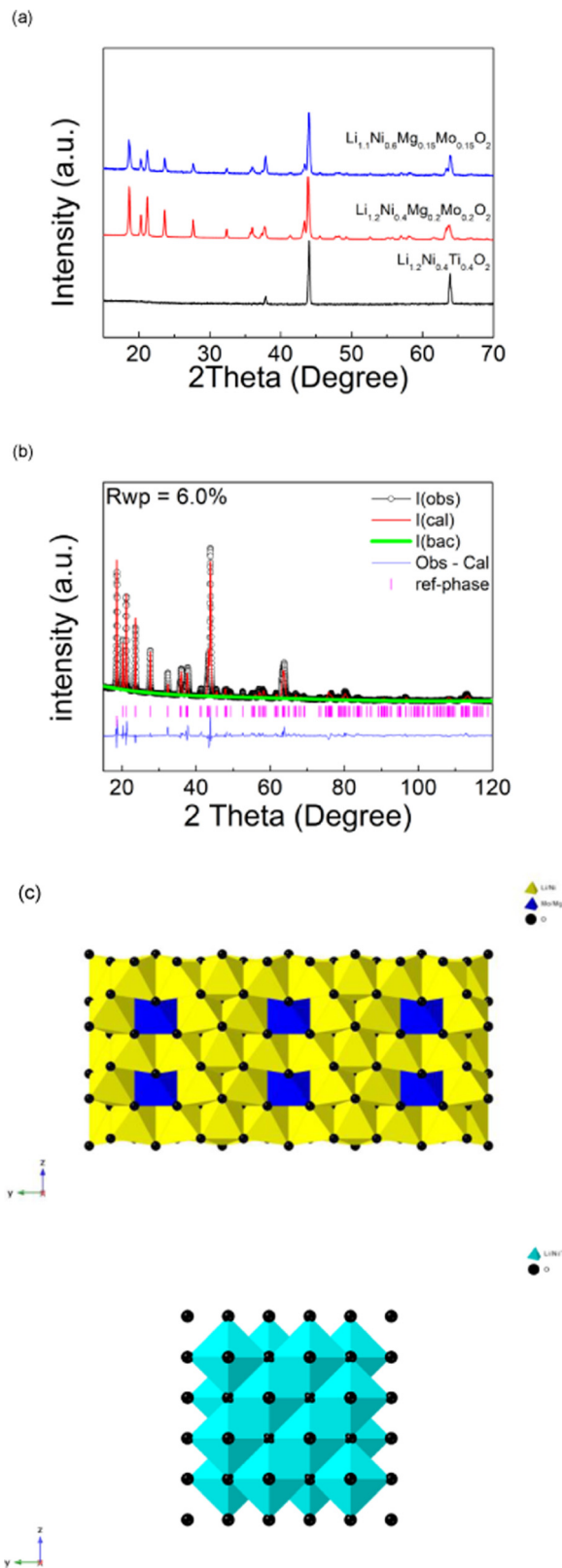


Fig. 1 (a) XRD patterns of  $\text{Li}_{1.2}\text{Ni}_{0.4}\text{Ti}_{0.4}\text{O}_2$ ,  $\text{Li}_{1.2}\text{Ni}_{0.4}\text{Mo}_{0.2}\text{Mg}_{0.2}\text{O}_2$  and  $\text{Li}_{1.1}\text{Ni}_{0.6}\text{Mo}_{0.15}\text{Mg}_{0.15}\text{O}_2$ . (b) Observed, calculated and difference profiles from structure refinement for  $\text{Li}_{1.2}\text{Ni}_{0.4}\text{Mo}_{0.2}\text{Mg}_{0.2}\text{O}_2$ . (c) Structure of  $\text{Li}_{1.2}\text{Ni}_{0.4}\text{Mo}_{0.2}\text{Mg}_{0.2}\text{O}_2$  and  $\text{Li}_{1.2}\text{Ni}_{0.4}\text{Ti}_{0.4}\text{O}_2$ .



ball mill (45 mL Si<sub>3</sub>N<sub>4</sub> pots with 10 mm diameter Si<sub>3</sub>N<sub>4</sub> balls), before mixing with PVDF and C65 in NMP at a 8:1:1 ratio at 1800 rpm/20 min to create cathode ink slurry. The slurry was coated onto Al foil with a 150 micrometer doctor blade and dried at 120 °C in a vacuum oven overnight before use. Li metal (Aldrich) was used as the anode, which was rolled and punched into 15 mm disks. The composition of the electrolyte (R&D 281, Soulbrain) was 1.0 M LiPF<sub>6</sub> in EC: EMC (ethylene carbonate/methyl carbonate, 3/7 V/V) with 1 wt% VC (Vinylene Carbonate) as an electrolyte additive. Microporous trilayer membrane (PP/PE/PP) (H1609, Celgard) was used as the separator.

The half cells using the components above were assembled as CR2032 coin cells in an argon-filled glove box. Galvanostatic charge/discharge with potential limitation (GVPL) measurements were conducted on the BCS805 cell tester (Bio-logic). The cells were cycled between 1.5 and 4.7/4.8 volts with constant current densities of 5–10 mA g<sup>-1</sup> at either room temperature or 40 °C.

### Scanning electron microscope (SEM)

Electrode samples were characterised by scanning electron microscopy (SEM, Apreo 2) utilising an EDT detector, with an accelerating voltage of 10 kV and spot size of 10. The working distance was set at around 10 mm. Magnifications of 200 and 500 were utilised for the observation of the samples. The elemental distributions on samples were measured by energy-dispersive X-ray spectroscopy (EDS) simultaneously with a fitted EDS detector (ChemSEM).

### X-Ray absorption spectroscopy (XAS)

Ni K-edge XAS spectra of NiO, LiNiO<sub>2</sub> and Li<sub>1.2</sub>Ni<sub>0.4</sub>Mo<sub>0.2</sub>Mg<sub>0.2</sub>O<sub>2</sub> at cut-off voltages (pristine, 4.2 V, 4.7 V, 2.2 V and 1.5 V), and Mo K-edge XAS spectra of MoO<sub>2</sub>, MoO<sub>3</sub> and Li<sub>1.2</sub>Ni<sub>0.4</sub>Mo<sub>0.2</sub>Mg<sub>0.2</sub>O<sub>2</sub> at cut-off voltages (pristine, 4.2 V, 4.7 V, 2.2 V and 1.5 V) were collected at I19 beamline, diamond light source.

## Results and discussions

### Structural characterisation

Li<sub>1.2</sub>Ni<sub>0.4</sub>Ti<sub>0.4</sub>O<sub>2</sub> was successfully synthesised through solid state reaction in air, and was shown to adopt a disordered rock

**Table 1** Refined structural parameters for Li<sub>1.2</sub>Ni<sub>0.4</sub>Mo<sub>0.2</sub>Mg<sub>0.2</sub>O<sub>2</sub>

Atom	<i>x</i>	<i>y</i>	<i>z</i>	Mult.	Occupancy	<i>u</i> <sub>iso</sub> (Å <sup>2</sup> )
Mg1	0	0	0	2	0.42	0.020(2)
Mo1	0	0	0	2	0.58	0.020(2)
O1	0.290(1)	0.340(1)	0.726(1)	8	1	0.020
O2	0.311(1)	0.5	0.172(1)	4	1	0.020
Ni1	0	0.663(1)	0	4	0.375	0.023(2)
Li1	0	0.663(1)	0	4	0.625	0.023(2)
Ni2	0	0.5	0.5	2	0.247	0.065(5)
Li2	0	0.5	0.5	2	0.753	0.065(5)
Ni3	0	0.168(2)	0.5	4	0.106	0.015(5)
Li3	0	0.168(2)	0.5	4	0.894	0.015(5)

Space group: *C2/m*, *a* = 5.0957(20) Å, *b* = 8.7638(5) Å, *c* = 5.0736(19) Å, *beta* = 110.18(1)°, *V* = 212.67 (1) Å<sup>3</sup>

salt structure (*a* = *b* = *c* = 4.1158(3) Å, *V* = 69.72 (1) Å<sup>3</sup>) in agreement with prior reports.<sup>24</sup> On replacing the Ti with a

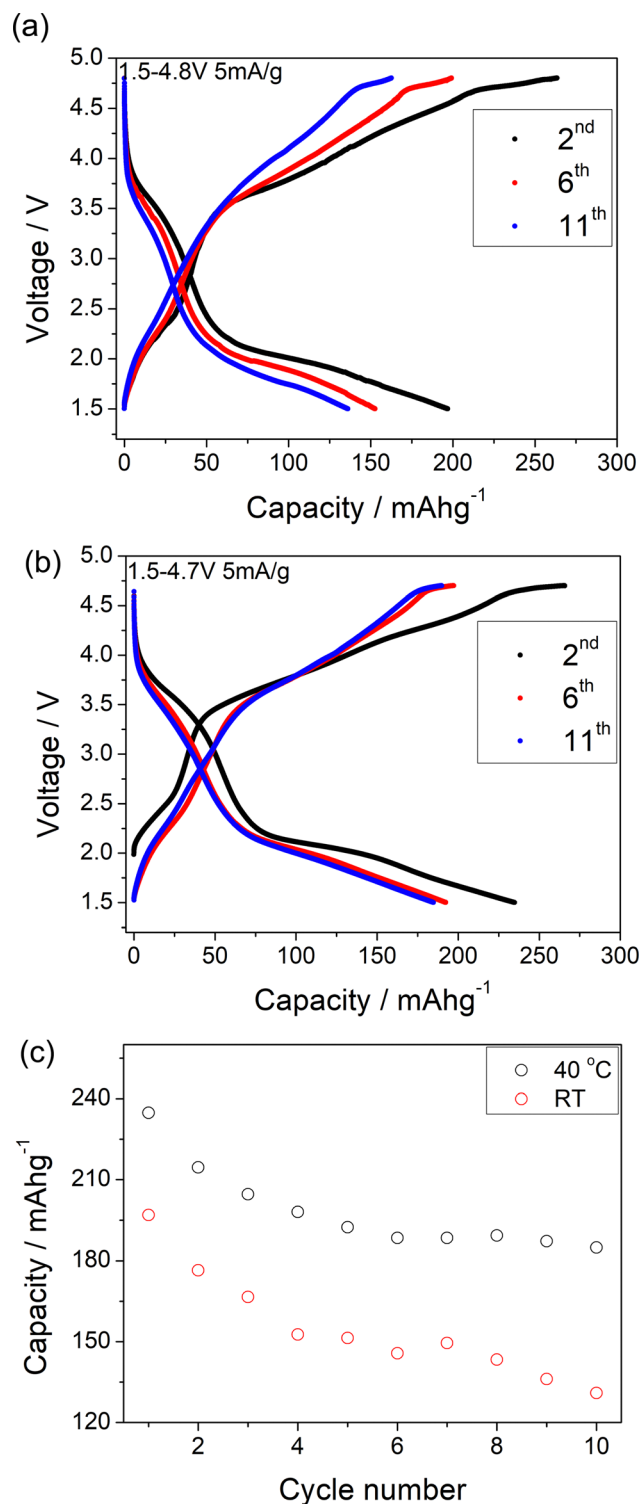


**Fig. 2** (a) Charge/discharge curves of Li<sub>1.2</sub>Ni<sub>0.4</sub>Mo<sub>0.2</sub>Mg<sub>0.2</sub>O<sub>2</sub> between 1.5 and 4.8 V at 5 mA g<sup>-1</sup> at RT. (b) Charge/discharge curves of Li<sub>1.2</sub>Ni<sub>0.4</sub>Mo<sub>0.2</sub>Mg<sub>0.2</sub>O<sub>2</sub> between 1.5 and 4.7 V at 5 mA g<sup>-1</sup> (≈C/40) at 40 °C. (c) Discharge capacity retention of Li<sub>1.2</sub>Ni<sub>0.4</sub>Mo<sub>0.2</sub>Mg<sub>0.2</sub>O<sub>2</sub> cycled at room temperature and 40 °C.



charge balanced combination of Mg and Mo (to give  $\text{Li}_{1.2}\text{Ni}_{0.4}\text{Mo}_{0.2}\text{Mg}_{0.2}\text{O}_2$ ), a change from a disordered rocksalt to a cation ordered layered phase was observed, as shown in Fig. 1(a). The XRD patterns of this new cation ordered layered phases are similar to  $\text{Li}_4\text{MoNiO}_6$ ,  $\text{Li}_4\text{WNiO}_6$  and  $\text{Li}_4\text{TeNiO}_6$ , whose structures are derived from that shown by  $\text{Li}_5\text{ReO}_6$ . A further system with higher Ni content,  $\text{Li}_{1.1}\text{Ni}_{0.6}\text{Mo}_{0.15}\text{Mg}_{0.15}\text{O}_2$ , was also successfully prepared, and showed a similar XRD pattern (Fig. 1(a)).

Structure refinement of  $\text{Li}_{1.2}\text{Ni}_{0.4}\text{Mo}_{0.2}\text{Mg}_{0.2}\text{O}_2$  was carried out using the XRD data. The starting model used was  $\text{Li}_5\text{ReO}_6$  which has a monoclinic unit cell with  $C2/m$  space group. Re1 was replaced by Mo1/Mg1 while Ni1, Ni2 and Ni3 were added to Li1, Li2 and Li3 sites respectively. Constraints of the same atomic coordinates and  $U_{\text{iso}}$  values with overall full site occupancy were made for Mo1/Mg1 (occupancies were set 1 and 0 for Mo1 and Mg1), Ni1/Li1, Ni2/Li2 and Ni3/Li3.  $U_{\text{iso}}$  (atomic displacement parameters) of each atom was set to a default value,  $0.02 \text{ \AA}^2$  and the scale factor, background (6 terms of shifted Chebyshev function) and lattice parameters were refined at first. The atomic coordinates of Mo1/Mg1, O1 and

O2 were refined in turn and fixed after the convergency, followed by the refinement of the occupancies of Ni1/Li1, Ni2/Li2 and Ni3/Li3 (fixed after the convergency). The occupancies of Mo1/Mg1 were then refined which gave values of 0.58(1) for Mo1 and 0.42(1) for Mg1, which corresponds to all the Mo in the composition within errors and suggests that the remaining Mg was distributed on three Ni/Li sites. This observed preference of Mo on the (0,0,0) site is most likely the driving force for the change from the DRS to the layered phase.

To complete the structure refinement and to confirm that it was not a false structural minimum, the atomic positions of all atoms were then refined together along with the refinement of  $U_{\text{iso}}$  values of Mo1/Mg1, Ni1/Li1, Ni2/Li2 and Ni3/Li3 ( $U_{\text{iso}}$  values of O1 and O2 were fixed at  $0.2 \text{ \AA}^2$ ). The final refined composition corresponded to  $\text{Li}_{3.79(4)}\text{Ni}_{1.21(4)}\text{Mo}_{0.58(1)}\text{Mg}_{0.42(1)}\text{O}_6$  (or  $\text{Li}_{1.26(2)}\text{Ni}_{0.40(2)}\text{Mo}_{0.19(1)}\text{Mg}_{0.14(1)}\text{O}_2$ ), which given the complex composition (4 different cations) is in good agreement with the expected composition. The final refined structural parameters of are shown in Table 1. A comparison of the structure of this phase to that of  $\text{Li}_{1.2}\text{Ni}_{0.4}\text{Ti}_{0.4}\text{O}_2$  is shown in Fig. 1(c).

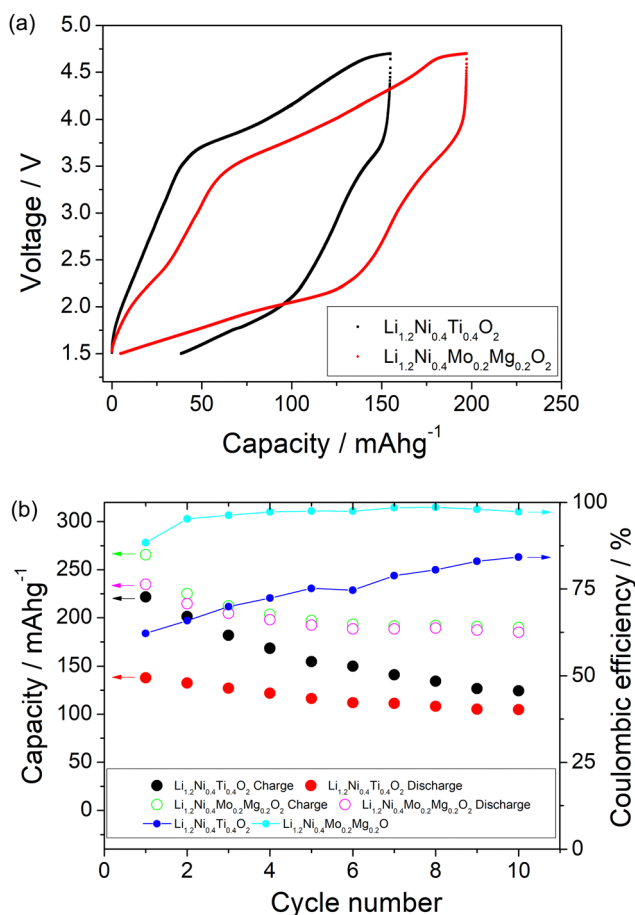


Fig. 3 (a) Charge/discharge curves of  $\text{Li}_{1.2}\text{Ni}_{0.4}\text{Ti}_{0.4}\text{O}_2$  and  $\text{Li}_{1.2}\text{Ni}_{0.4}\text{Mo}_{0.2}\text{Mg}_{0.2}\text{O}_2$  between 1.5 and 4.7 V at  $5 \text{ mA g}^{-1}$  at  $40 \text{ }^\circ\text{C}$ , illustrating higher capacity and slightly reduced hysteresis for the latter. (b) Charge/discharge capacity retention and coulombic efficiency of  $\text{Li}_{1.2}\text{Ni}_{0.4}\text{Ti}_{0.4}\text{O}_2$  and  $\text{Li}_{1.2}\text{Ni}_{0.4}\text{Mo}_{0.2}\text{Mg}_{0.2}\text{O}_2$  cycled at  $40 \text{ }^\circ\text{C}$ .

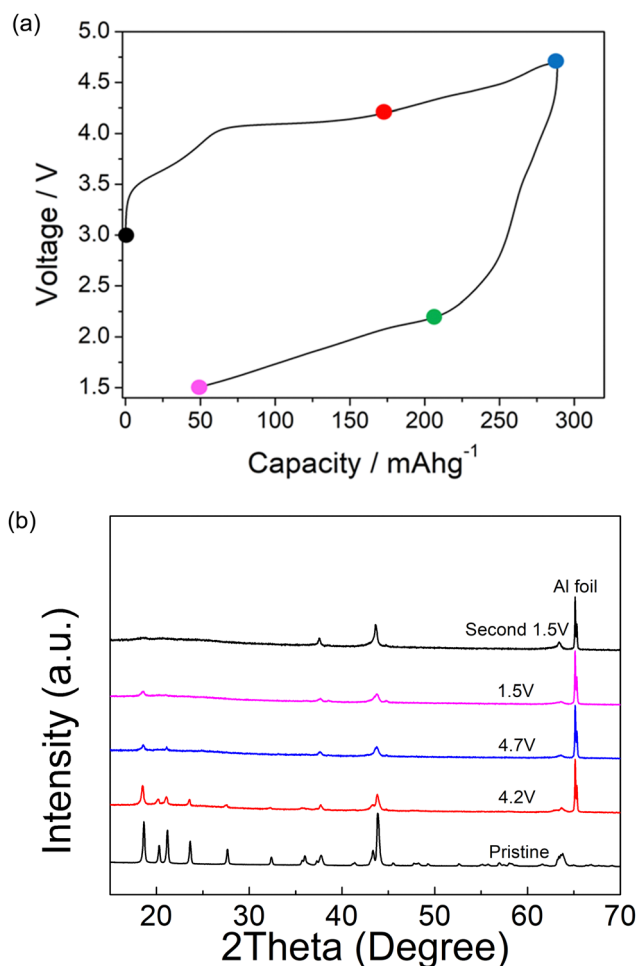


Fig. 4 (a) schematic cut off points for *ex situ* characterization of  $\text{Li}_{1.2}\text{Ni}_{0.4}\text{Mo}_{0.2}\text{Mg}_{0.2}\text{O}_2$  during the cycling of the cell. (b) *Ex situ* XRD of  $\text{Li}_{1.2}\text{Ni}_{0.4}\text{Mo}_{0.2}\text{Mg}_{0.2}\text{O}_2$  at these different cut-off voltages.



### Electrochemical testing

**Li<sub>1.2</sub>Ni<sub>0.4</sub>Mo<sub>0.2</sub>Mg<sub>0.2</sub>O<sub>2</sub>.** The theoretical capacity of Li<sub>1.2</sub>Ni<sub>0.4</sub>Mo<sub>0.2</sub>Mg<sub>0.2</sub>O<sub>2</sub> is 366 mA h g<sup>-1</sup> assuming all the Li can be extracted from the cathode framework. The electrochemical data for this system showed a high charge capacity of 275 mA h g<sup>-1</sup> at room temperature and 300 mA h g<sup>-1</sup> at 40 °C when charged to 4.8 V, thus approaching this value. However, the discharge capacity was found to be limited to 200 mA h g<sup>-1</sup> (room temperature) and a large hysteresis is seen, which can be attributed to factors limiting the kinetics of the electrochemical process (Fig. 2(a)). Furthermore, the reversible capacity decreased to 132 mA h g<sup>-1</sup> after 10 cycles (66% retention) which may be attributed to the irreversible oxygen loss or decomposition of electrolyte at high voltage. To improve the electrochemical performance further, the cell was measured at elevated temperature (40 °C) and a slightly lower cut-off voltage (4.7 V) was chosen. As shown in Fig. 2(b), the reversible capacity is improved, and reaches 237 mA h g<sup>-1</sup> on delithiation in the 2nd cycle with a capacity fade to 195 mA h g<sup>-1</sup> by the 11th cycle (an initial 1st formation cycle is shown in Fig. S2, ESI<sup>†</sup>), suggesting that O<sub>2</sub> loss may be the main factor affecting the capacity fade in this material. Thus, in addition to the higher starting capacity, the capacity retention rate was improved (from 66% to 83% after 10 cycles) (Fig. 2(c)), indicating the improved electrochemical kinetics and enhanced stability with the higher temperature.

A comparison of the charge/discharge curves of Li<sub>1.2</sub>Ni<sub>0.4</sub>Ti<sub>0.4</sub>O<sub>2</sub> and Li<sub>1.2</sub>Ni<sub>0.4</sub>Mo<sub>0.2</sub>Mg<sub>0.2</sub>O<sub>2</sub> is shown in Fig. 3(a).

Both samples show a high degree of hysteresis between charge/discharge, although this is slightly smaller for Li<sub>1.2</sub>Ni<sub>0.4</sub>Mo<sub>0.2</sub>Mg<sub>0.2</sub>O<sub>2</sub> and this latter sample also delivered increased discharged capacity at low voltage compared to that of Li<sub>1.2</sub>Ni<sub>0.4</sub>Ti<sub>0.4</sub>O<sub>2</sub>. The charge/discharge retention of Li<sub>1.2</sub>Ni<sub>0.4</sub>Ti<sub>0.4</sub>O<sub>2</sub> and Li<sub>1.2</sub>Ni<sub>0.4</sub>Mo<sub>0.2</sub>Mg<sub>0.2</sub>O<sub>2</sub> are shown in Fig. 3(b). The Li<sub>1.2</sub>Ni<sub>0.4</sub>Mo<sub>0.2</sub>Mg<sub>0.2</sub>O<sub>2</sub> displays improved cycling performance with a capacity retention of 83% compared to 77% for Li<sub>1.2</sub>Ni<sub>0.4</sub>Ti<sub>0.4</sub>O<sub>2</sub>. Additionally, the Li<sub>1.2</sub>Ni<sub>0.4</sub>Mo<sub>0.2</sub>Mg<sub>0.2</sub>O<sub>2</sub> cathode offered a better coulombic efficiency (~84% and 98% for Li<sub>1.2</sub>Ni<sub>0.4</sub>Ti<sub>0.4</sub>O<sub>2</sub> and Li<sub>1.2</sub>Ni<sub>0.4</sub>Mo<sub>0.2</sub>Mg<sub>0.2</sub>O<sub>2</sub>), indicating the improvement in the electrochemical performance compared to Li<sub>1.2</sub>Ni<sub>0.4</sub>Ti<sub>0.4</sub>O<sub>2</sub>.

In Li<sub>1.2</sub>Ni<sub>0.4</sub>Mo<sub>0.2</sub>Mg<sub>0.2</sub>O<sub>2</sub>, the Mg is likely not involved in the electrochemical intercalation/deintercalation but shares the sites with both Mo and Li/Ni, and so may hinder the Li migration during the cycling and lead to the poor kinetics. In order to try to improve the performance, a further sample Li<sub>1.1</sub>Ni<sub>0.6</sub>Mo<sub>0.15</sub>Mg<sub>0.15</sub>O<sub>2</sub>, with higher Ni content and less Mg content was prepared in an attempt to increase the Ni redox contribution to the capacity. The position of the X-ray diffraction peaks in Li<sub>1.2</sub>Ni<sub>0.4</sub>Mo<sub>0.2</sub>Mg<sub>0.2</sub>O<sub>2</sub> and Li<sub>1.1</sub>Ni<sub>0.6</sub>Mo<sub>0.15</sub>Mg<sub>0.15</sub>O<sub>2</sub> are similar (Fig. 1), indicating these two structures have the same space group. The patterns show some differences in peak intensities, which may relate to the different compositions (increase in Ni, reduction in Li, Mg, Mo content) as well as some difference in the distribution of the cations in the structure. The samples also show different FWHM, which may relate to different particle sizes due to the slight difference in the temperature (925 vs. 950 °C) needed to prepare these two phases. With the increased Ni content

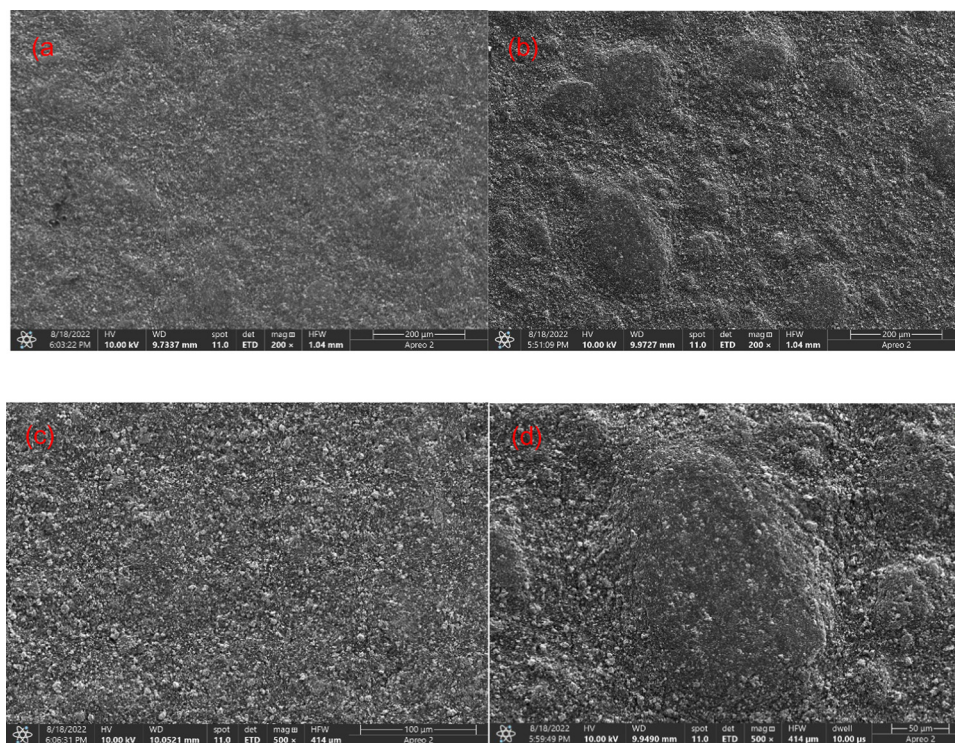


Fig. 5 (a) and (c) SEM of pristine Li<sub>1.2</sub>Ni<sub>0.4</sub>Mo<sub>0.2</sub>Mg<sub>0.2</sub>O<sub>2</sub> at 200 and 500× magnification (b) and (d) SEM of cycled Li<sub>1.2</sub>Ni<sub>0.4</sub>Mo<sub>0.2</sub>Mg<sub>0.2</sub>O<sub>2</sub> at 200 and 500× magnification.



and decreased Mg content, the results suggested an improvement in the redox kinetics of  $\text{Li}_{1.1}\text{Ni}_{0.6}\text{Mo}_{0.15}\text{Mg}_{0.15}\text{O}_2$ , allowing for a good capacity to be achieved even at RT with a higher current density ( $10 \text{ mA g}^{-1}$ ), although there was still significant capacity fade observed (the electrochemical data are shown in the Fig. S3 and S4, ESI†).

### Ex situ characterisation

Ex situ X-ray diffraction characterization of  $\text{Li}_{1.2}\text{Ni}_{0.4}\text{Mg}_{0.2}\text{Mo}_{0.2}\text{O}_2$  was carried out at different cut-off voltages (uncharged state, 4.2 V, 4.7 V and 1.5 V) in order to understand the redox mechanism during the cycling of this layered system (Fig. 4). The ordered structure associated with peaks at low angles ( $\sim 30$  degree) was retained to 4.2 V, although these peaks started to decrease in intensity with increasing cut-off voltage at 4.5 and 4.7 V. These peaks almost fully disappeared for the second cycle and the ordered layered structure was observed to transform into the disordered rocksalt structure. This observation indicates an irreversible phase change associated with the rearrangement of cations, such as Mo migration, and possible oxygen loss in the structure during the cycling. In the case of the latter, any oxygen vacancies created may facilitate cation migration aiding this transformation to the DRS structure. The large hysteresis may therefore be related to this additional slow cation movement, for example octahedral  $\text{Mo}^{6+}$  to tetrahedral  $\text{Mo}^{4+}$ , similar to the reported  $\text{Cr}^{6+}/\text{Cr}^{4+}$  migration within  $\text{Li}_{1.2}\text{Ni}_{0.1}\text{Ti}_{0.5}\text{Cr}_{0.2}\text{O}_2$ .<sup>22</sup> The hysteresis was reduced with increased temperature (shown in Fig. 2), which can most likely be related to the faster cation migration at elevated temperature. The SEM image of pristine and post materials (after 2 cycles) showed a change in morphology, as shown in Fig. 5. The electrode before cycling shows a flat top surface (Fig. 5(a) and (c)) and electrode after cycling shows a rougher surface with raised particle clusters. The raised particle clusters are very likely formed by volume change during repeating lithiation and delithiation, which is common for Li-rich layered oxide electrodes, as shown in previously for  $\text{Li}_{1.2}\text{Ni}_{0.13}\text{Mn}_{0.54}\text{Co}_{0.13}\text{O}_2$ .<sup>32</sup> The raised particle clusters may lead to partial delamination and capacity decay.

The  $dQ/dV$  vs. voltage plots of  $\text{Li}_{1.2}\text{Ni}_{0.4}\text{Ti}_{0.4}\text{O}_2$  and  $\text{Li}_{1.2}\text{Ni}_{0.4}\text{Mo}_{0.2}\text{Mg}_{0.2}\text{O}_2$  are shown in Fig. 6(a). The main oxidation peak at  $\sim 3.85$  V associated with  $\text{Ni}^{3+}/\text{Ni}^{4+}$  redox was observed for both samples and the corresponding  $\text{Ni}^{4+}/\text{Ni}^{3+}$  reduction peak was seen at  $\sim 3.6$  V. When charging above 4 V, an additional small oxidation peak was seen at  $\sim 4.3$  V, which may be attributed to the bulk oxygen redox or  $\text{O}_2$  release from the surface of particles. In terms of the redox peaks at low voltage, a reduction peak attributed to  $\text{Mo}^{6+}/\text{Mo}^{4+}$  at  $\sim 2.1$  V and the corresponding oxidation peak of  $\text{Mo}^{4+}/\text{Mo}^{6+}$  at  $\sim 2.3$  V were seen for  $\text{Li}_{1.2}\text{Ni}_{0.4}\text{Mo}_{0.2}\text{Mg}_{0.2}\text{O}_2$ , which is consistent with the XAS results (see below). In comparison, two very small reduction peaks at  $\sim 1.9$  and  $1.7$  V were observed for the  $\text{Li}_{1.2}\text{Ni}_{0.4}\text{Ti}_{0.4}\text{O}_2$  which may be related to the reduction of  $\text{Ti}^{4+}$  and  $\text{Ni}^{3+}$ . The lower voltage feature was not reversible, with no oxidation peak of  $\text{Ti}^{3+}$  below 3 V observed upon recharging.

In order to identify the redox mechanism during the cycling, Ni K-edge and Mo K-edge XAS were collected at different cut-off

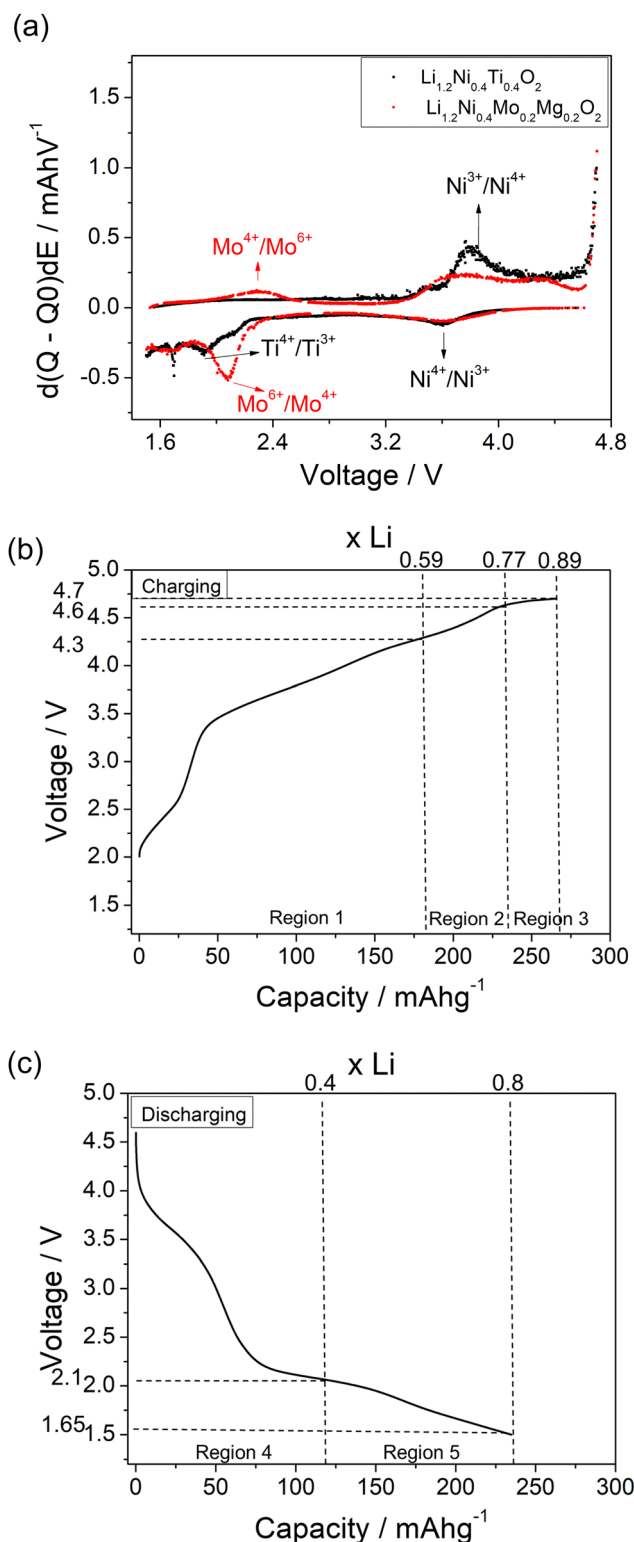


Fig. 6 (a)  $dQ/dV$  curve of  $\text{Li}_{1.2}\text{Ni}_{0.4}\text{Ti}_{0.4}\text{O}_2$  and  $\text{Li}_{1.2}\text{Ni}_{0.4}\text{Mo}_{0.2}\text{Mg}_{0.2}\text{O}_2$  at the fifth cycle. (b) Charge curve of  $\text{Li}_{1.2}\text{Ni}_{0.4}\text{Mo}_{0.2}\text{Mg}_{0.2}\text{O}_2$  between 1.5 and 4.7 V at  $5 \text{ mA g}^{-1}$  at  $40^\circ\text{C}$ . (c) Discharge curve of  $\text{Li}_{1.2}\text{Ni}_{0.4}\text{Mo}_{0.2}\text{Mg}_{0.2}\text{O}_2$  between 1.5 and 4.7 V at  $5 \text{ mA g}^{-1}$  at  $40^\circ\text{C}$ .



voltages. As shown in Fig. 6(b), during the 2nd charge of the cell,  $\sim 180 \text{ mA h g}^{-1}$  capacity was obtained at 4.3 cut-off voltage (region 1), which is attributed to both  $\text{Mo}^{4+}/\text{Mo}^{6+}$  and  $\text{Ni}^{3+}/\text{Ni}^{4+}$  redox ( $180 \text{ mA h g}^{-1}$  accounts for  $\sim 0.6 \text{ Li}$ ) as indicated in the  $dQ/dV$  plot (Fig. 6a). Ni K-edge XAS data (Fig. 7) also supported this result with the peak at 8353 eV slightly shifting to high energy, illustrating the oxidation of  $\text{Ni}^{3+}$ . The additional  $55 \text{ mA h g}^{-1}$  capacity between 4.3 V and 4.6 V (region 2) associated with the broad peak at 4.35 V in the  $dQ/dV$  plot was attributed to either bulk oxygen redox, or  $\text{O}_2$  loss from the surface of particles. The change of slope in the voltage profile as well as a sharp peak in the  $dQ/dV$  plot above 4.6 V (region 3) was observed, which is a good indication of electrolyte decomposition. The electrolyte decomposition during the electrochemical reaction will usually generate unwanted gas, increase the internal cell pressure, and the decomposition products of the electrolyte can further react with the SEI layer or cathode material, thus generally leading to the degradation of the electrochemical performance.

$240 \text{ mA h g}^{-1}$  capacity was then gained on discharging in the 2nd cycle, which can be divided into two regions at 2.1 V

(Fig. 6(c)). In the region 4, the voltage dropped sharply to 3.9 V without any redox peaks observed in the  $dQ/dV$  plot. The only redox peak observed over this region was the  $\text{Ni}^{4+}/\text{Ni}^{3+}$  reduction peak at  $\sim 3.6 \text{ V}$ , which indicates the  $\sim 120 \text{ mA h g}^{-1}$  capacity was attributed to Ni redox. In the region 5, the main reduction peak ( $\text{Mo}^{6+}/\text{Mo}^{4+}$ ) at 2.1 V and a tiny peak at 1.65 V which may be due to partially reduction  $\text{Mo}^{4+}$  or  $\text{Ni}^{3+}$  were observed. This suggests that the low voltage capacity is mainly from  $\text{Mo}^{6+}/\text{Mo}^{4+}$  redox ( $100 \text{ mA h g}^{-1}$ ). This is also supported by the Mo k-edge XAS (Fig. 8) where initially there was no change in the spectra on charge to 4.7 V in the 1st cycle, indicating only  $\text{Mo}^{6+}$ . However, on discharging, the peak intensities at 19930 and 19995 eV (representative for  $\text{Mo}^{4+}$ ) increased slightly compared to the pristine material, supporting the presence of  $\text{Mo}^{6+}/\text{Mo}^{4+}$  redox in subsequent cycle. The reduction of  $\text{Mo}^{6+}$  could then trigger the possible migration of Mo to tetrahedral sites, which may then move back to extracted  $\text{Li}^+$  sites on delithiation and thus also facilitate the transition from a layered phase to disordered rocksalt phase on cycling, and the corresponding hysteresis in the voltage profile observed. Compared to olivine  $\text{LiFePO}_4$  ( $165 \text{ mA h g}^{-1}$ ), spinel  $\text{LiMn}_2\text{O}_4$

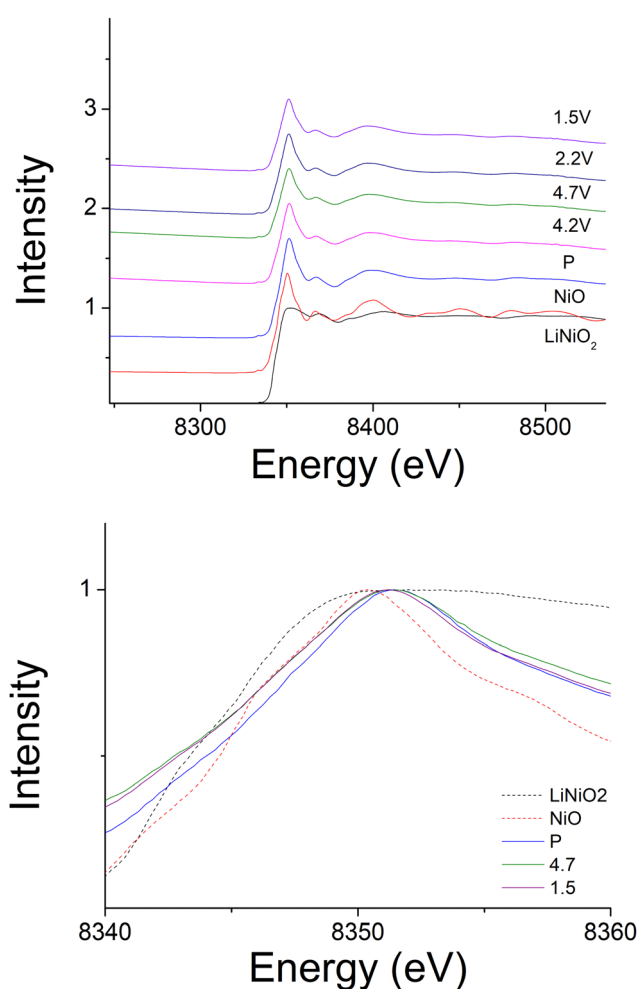


Fig. 7 Ex situ Ni-edge XAS of  $\text{Li}_{1.2}\text{Ni}_{0.4}\text{Mo}_{0.2}\text{Mg}_{0.2}\text{O}_2$  at different cut-off voltages.

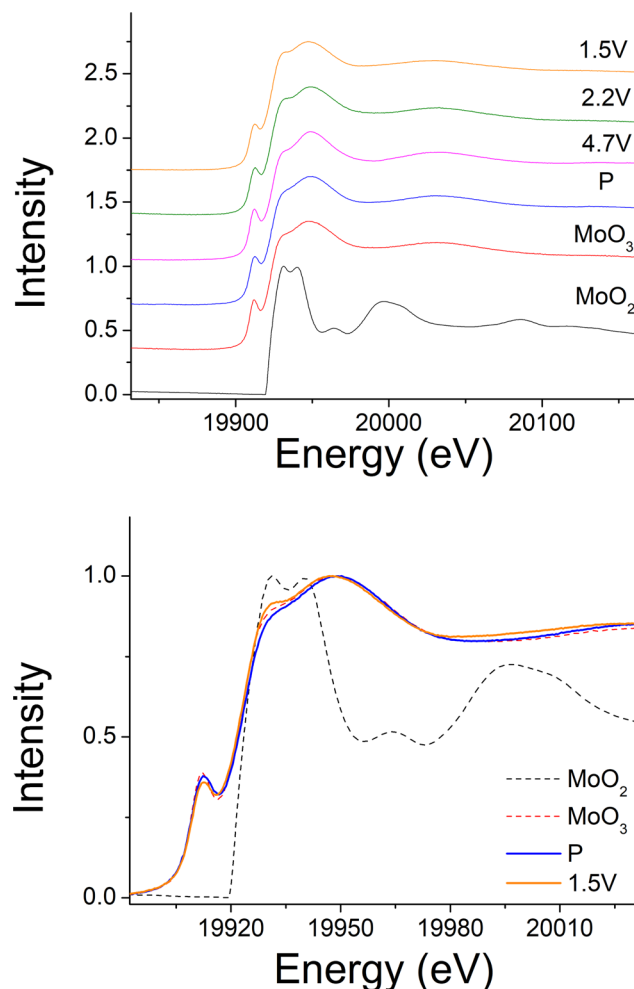


Fig. 8 Ex situ Mo-edge XAS of  $\text{Li}_{1.2}\text{Ni}_{0.4}\text{Mo}_{0.2}\text{Mg}_{0.2}\text{O}_2$  at different cut-off voltages.



(120 mA h g<sup>-1</sup>) and layered LiNi<sub>0.33</sub>Mn<sub>0.33</sub>Co<sub>0.33</sub>O<sub>2</sub> materials (170 mA h g<sup>-1</sup>),<sup>33</sup> this new material showed improved capacity (~237 mA h g<sup>-1</sup> at first cycle and 195 mA h g<sup>-1</sup> after 10 cycles). However, the material suffers from slow kinetics, large hysteresis and capacity fade, and so further work is needed to overcome these issues, for example the investigation of additional substitution strategies, such as F doping.

## Conclusions

In conclusion, through a dual cation substitution strategy replacing Ti with Mo and Mg, new cation ordered layered oxides with composition Li<sub>1.2</sub>Ni<sub>0.4</sub>Mo<sub>0.2</sub>Mg<sub>0.2</sub>O<sub>2</sub> and Li<sub>1.1</sub>Ni<sub>0.6</sub>Mo<sub>0.15</sub>Mg<sub>0.15</sub>O<sub>2</sub> were successfully prepared. Li<sub>1.2</sub>Ni<sub>0.4</sub>Mo<sub>0.2</sub>Mg<sub>0.2</sub>O<sub>2</sub> delivered up to 195 mA h g<sup>-1</sup> discharge capacity after 10 cycles, which was higher than observed for the corresponding Li<sub>1.2</sub>Ni<sub>0.4</sub>Ti<sub>0.4</sub>O<sub>2</sub>. *Ex situ* XRD indicated an irreversible phase change to a disordered rocksalt phase on cycling. *Ex situ* XAS and dQ/dV studies showed Ni<sup>3+</sup>/Ni<sup>4+</sup> and Mo<sup>4+</sup>/Mo<sup>6+</sup> redox as well as possible oxygen redox or O<sub>2</sub> release happening on delithiation, while Ni<sup>4+</sup>/Ni<sup>3+</sup> and Mo<sup>6+</sup>/Mo<sup>4+</sup> redox occurred on lithiation. Structure refinement suggested that high valence dopant Mo<sup>6+</sup> directs the cation ordering in as-prepared Li<sub>1.2</sub>Ni<sub>0.4</sub>Mo<sub>0.2</sub>Mg<sub>0.2</sub>O<sub>2</sub>, and the irreversible phase change to disordered rock salt on cycling is attributed to slow cation movement (*e.g.* Mo) to new sites. Overall, this work shows both the possibilities and challenges in designing new cathode materials in that the substitution strategy successfully led to a new modified cation ordered layered structure, which then reverted back to disordered rock salt on cycling.

## Conflicts of interest

The authors declare no conflict of interest.

## Acknowledgements

We would like to thank Faraday Institution CATMAT (FIRG016) and NEXTRODE (FIRG015) projects for funding. We would like to thank XAS data collection by Dr Giannantonio Cibir with Energy BAG scheme in Diamond. Raw experimental data can be found at <https://doi.org/10.25500/edata.bham.00000892>.

## References

- J.-M. Tarascon and M. Armand, *Nature*, 2001, **414**, 359–367.
- J. B. Goodenough and K. S. Park, *J. Am. Chem. Soc.*, 2013, **135**, 1167–1176.
- A. D. Robertson and P. G. Bruce, *Chem. Mater.*, 2003, **15**, 1984–1992.
- A. D. Robertson and P. G. Bruce, *Chem. Commun.*, 2002, 2790–2791, DOI: [10.1039/b207945c](https://doi.org/10.1039/b207945c).
- H. Huang, S. C. Yin and L. F. Nazar, *Electrochem. Solid-State Lett.*, 2001, **4**, A170–A172.
- M. M. Thackeray, W. I. F. David, P. G. Bruce and J. B. Goodenough, *Mater. Res. Bull.*, 1983, **18**, 461–472.
- K. Luo, M. R. Roberts, R. Hao, N. Guerrini, D. M. Pickup, Y. S. Liu, K. Edstrom, J. Guo, A. V. Chadwick, L. C. Duda and P. G. Bruce, *Nat. Chem.*, 2016, **8**, 684–691.
- R. A. House, G. J. Rees, M. A. Pérez-Osorio, J.-J. Marie, E. Boivin, A. W. Robertson, A. Nag, M. Garcia-Fernandez, K.-J. Zhou and P. G. Bruce, *Nat. Energy*, 2020, **5**, 777–785.
- T. Matsuhara, Y. Tsuchiya, K. Yamanaka, K. Mitsuhara, T. Ohta and N. Yabuuchi, *Electrochem.*, 2016, **84**, 797–801.
- E. McCalla, M. T. Sougrati, G. Rousse, E. J. Berg, A. Abakumov, N. Recham, K. Ramesha, M. Sathiya, R. Dominko, G. Van Tendeloo, P. Novak and J. M. Tarascon, *J. Am. Chem. Soc.*, 2015, **137**, 4804–4814.
- B. Li and D. Xia, *Adv. Mater.*, 2017, **29**, 1701054.
- G. Assat and J.-M. Tarascon, *Nat. Energy*, 2018, **3**, 373–386.
- M. Han, J. Jiao, Z. Liu, X. Shen, Q. Zhang, H. J. Lin, C. T. Chen, Q. Kong, W. K. Pang, Z. Guo, R. Yu, L. Gu, Z. Hu, Z. Wang and L. Chen, *Adv. Energy Mater.*, 2020, **10**, 1903634.
- D. Eum, B. Kim, S. J. Kim, H. Park, J. Wu, S. P. Cho, G. Yoon, M. H. Lee, S. K. Jung, W. Yang, W. M. Seong, K. Ku, O. Tamwattana, S. K. Park, I. Hwang and K. Kang, *Nat. Mater.*, 2020, **19**, 419–427.
- Q. Jacquet, A. Iadecola, M. Saubanere, H. Li, E. J. Berg, G. Rousse, J. Cabana, M. L. Doublet and J. M. Tarascon, *J. Am. Chem. Soc.*, 2019, **141**, 11452–11464.
- R. A. House, U. Maitra, L. Jin, J. G. Lozano, J. W. Somerville, N. H. Rees, A. J. Naylor, L. C. Duda, F. Massel, A. V. Chadwick, S. Ramos, D. M. Pickup, D. E. McNally, X. Lu, T. Schmitt, M. R. Roberts and P. G. Bruce, *Chem. Mater.*, 2019, **31**, 3293–3300.
- R. A. House, U. Maitra, M. A. Perez-Osorio, J. G. Lozano, L. Jin, J. W. Somerville, L. C. Duda, A. Nag, A. Walters, K. J. Zhou, M. R. Roberts and P. G. Bruce, *Nature*, 2020, **577**, 502–508.
- R. A. House, J.-J. Marie, M. A. Pérez-Osorio, G. J. Rees, E. Boivin and P. G. Bruce, *Nat. Energy*, 2021, **6**, 781–789.
- Z. Lun, B. Ouyang, D. H. Kwon, Y. Ha, E. E. Foley, T. Y. Huang, Z. Cai, H. Kim, M. Balasubramanian, Y. Sun, J. Huang, Y. Tian, H. Kim, B. D. McCloskey, W. Yang, R. J. Clement, H. Ji and G. Ceder, *Nat. Mater.*, 2021, **20**, 214–221.
- R. J. Clément, Z. Lun and G. Ceder, *Energy Environ. Sci.*, 2020, **13**, 345–373.
- K. Zhou, S. Zheng, H. Liu, C. Zhang, H. Gao, M. Luo, N. Xu, Y. Xiang, X. Liu, G. Zhong and Y. Yang, *ACS Appl. Mater. Interfaces*, 2019, **11**, 45674–45682.
- J. Huang, P. Zhong, Y. Ha, D.-H. Kwon, M. J. Crafton, Y. Tian, M. Balasubramanian, B. D. McCloskey, W. Yang and G. Ceder, *Nat. Energy*, 2021, **6**, 706–714.
- H. Ji, A. Urban, D. A. Kitchaev, D. H. Kwon, N. Artrith, C. Ophus, W. Huang, Z. Cai, T. Shi, J. C. Kim, H. Kim and G. Ceder, *Nat. Commun.*, 2019, **10**, 592.
- L. Zhang, H. Noguchi, D. Li, T. Muta, X. Wang, M. Yoshio and I. Taniguchi, *J. Power Sources*, 2008, **185**, 534–541.
- Y. Liu, S. Zheng, H. Wan, A. Dou, D. Chu and M. Su, *J. Alloys Compd.*, 2017, **728**, 659–668.





- 26 Z. Yu, X. Qu, A. Dou, M. Su, Y. Liu and F. Wu, *ACS Appl. Mater. Interfaces*, 2019, **11**, 35777–35787.
- 27 J. Lee, D.-H. Seo, M. Balasubramanian, N. Twu, X. Li and G. Ceder, *Energy Environ. Sci.*, 2015, **8**, 3255–3265.
- 28 Z. N. Taylor, A. J. Perez, J. A. Coca-Clemente, F. Braga, N. E. Drewett, M. J. Pitcher, W. J. Thomas, M. S. Dyer, C. Collins, M. Zanella, T. Johnson, S. Day, C. Tang, V. R. Dhanak, J. B. Claridge, L. J. Hardwick and M. J. Rosseinsky, *J. Am. Chem. Soc.*, 2019, **141**, 7333–7346.
- 29 N. Yabuuchi, Y. Tahara, S. Komaba, S. Kitada and Y. Kajiya, *Chem. Mater.*, 2016, **28**, 416–419.
- 30 M. Sathiya, K. Ramesha, G. Rouse, D. Foix, D. Gonbeau, K. Guruprakash, A. S. Prakash, M. L. Doublet and J. M. Tarascon, *Chem. Commun.*, 2013, **49**, 11376–11378.
- 31 B. H. Toby, *J. Appl. Crystallogr.*, 2001, **34**, 210–213.
- 32 T. C. Liu, J. J. Liu, L. X. Li, L. Yu, J. C. Diao, T. Zhou, S. N. Li, A. Dai, W. G. Zhao, S. Y. Xu, Y. Ren, L. G. Wang, T. P. Wu, R. Qi, Y. G. Xiao, J. X. Zheng, W. Cha, R. Harder, I. Robinson, J. G. Wen, J. Lu, F. Pan and K. Amine, *Nature*, 2022, **606**, 305–312.
- 33 N. Nitta, F. X. Wu, J. T. Lee and G. Yushin, *Mater. Today*, 2015, **18**, 252–264.

